Exact and Approximate Fourier Rebinning Algorithms for the Solution of the Data Truncation Problem in 3-D PET

Fayçal Ben Bouallègue*, Jean-François Crouzet, Claude Comtat, *Member, IEEE*, Marjolaine Fourcade, Bijan Mohammadi, and Denis Mariano-Goulart

***Abstract*—This paper presents an extended 3-D exact rebinning formula in the Fourier space that leads to an iterative reprojection algorithm (iterative FOREPROJ), which enables the estimation of unmeasured oblique projection data on the basis of the whole set of measured data. In first approximation, this analytical formula also leads to an extended Fourier rebinning equation that is the basis for an approximate reprojection algorithm (extended FORE). These algorithms were evaluated on numerically simulated 3-D positron emission tomography (PET) data for the solution of the truncation problem, i.e., the estimation of the missing portions in the oblique projection data, before the application of algorithms that require complete projection data such as some rebinning methods (FOREX) or 3-D reconstruction algorithms (3DRP or direct Fourier methods). By taking advantage of all the 3-D data statistics, the iterative FOREPROJ reprojection provides a reliable alternative to the classical FOREPROJ method, which only exploits the low-statistics nonoblique data. It significantly improves the quality of the external reconstructed slices without loss of spatial resolution. As for the approximate extended FORE algorithm, it clearly exhibits limitations due to axial interpolations, but will require clinical studies with more realistic measured data in order to decide on its pertinence.**

***Index Terms*—Fourier rebinning, image reconstruction, medical imaging, positron emission tomography (PET), reprojection.**

I. Introduction

FOLLOWING the development in the late 1980s of a new generation of multiring scanners, the field of application of positron emission tomography (PET) was extended to 3-D medical imaging, which led to the now widespread utilization of volume PET scanners. In this context arose the problematics of 3-D data acquisition and reconstruction [1]–[7]. Many techniques and algorithms have been implemented to take advantage of the redundancy of 3-D PET data, among which the so-called rebinning algorithms [8]–[15].

These rebinning algorithms can be used to rearrange the set of 3-D data acquired by the PET scanner into a stack of 2-D sinograms that correspond to the transaxial slices. In the (realistic) case of noisy data acquisition, this processing increases the statistics and thus the signal-to-noise ratio (SNR) in the reconstructed slices compared with that obtained after simple 2-D slice by slice acquisition. Moreover, these rebinning algorithms are much less time-consuming than other methods which exploit the redundancy of 3-D projections (fully 3-D algorithms), such as the classical 3-D filtered back projection (3DRP) method [4], [17]. The simplest way to increase the signal to noise ratio using rebinning techniques is either to assign each oblique line of response (LOR) between two detectors in coincidence to the transaxial plane lying midway axially between these two detectors [single-slice rebinning, (SSRB)] [6], [8], [10], [16] or to let each oblique LOR contribute to all the transverse planes it intersects (multislice rebinning, MSRB) [9], [10]. However, SSRB provides poor results when the distribution to be reconstructed is not localized near the axis of the scanner, whereas MSRB becomes less stable as the 3-D data grow noisy [14], [17], [18]. In the 1990s, innovative rebinning algorithms based on an analytical factorization method in the 3-D Fourier space were proposed [11]–[15], namely the Fourier rebinning (FORE) [11] and the exact Fourier rebinning (FOREX) [12], [14] algorithms. FORE shows good accuracy as well as stability in the presence of noise [19]. In addition, it allows a significant speedup in the reconstruction, hence providing a reliable alternative to fully 3-D reconstruction. However, the approximation it involves is no longer valid at wide angles, making it unsuitable for large aperture scanners.

Besides the purpose of computing 2-D rebinned projection data with improved SNR, the general frame of rebinning can also be used to synthesize the projection data that cannot be measured with the usual cylindrical PET scanners, i.e. to solve the data truncation problem in 3-D PET. This kind of rebinning can be regarded as an alternative to the classical forward-projection step. This procedure has been proposed as a preprocessing step (FOREPROJ) before using an exact rebinning algorithm (FOREX) that requires axial invariance in the 3-D projection data [14].

The estimation of unmeasured oblique projection data is also necessary for analytical 3-D reconstruction algorithms such as 3DRP or direct Fourier methods (DFM). Recently, in both the

Manuscript received December 8, 2006; revised February 23, 2007. *Asterisk indicates corresponding author.*

*F. Ben Bouallègue is with Montpellier II University, Mathematics and Modeling Institute, Place Eugène Bataillon, Montpellier 34095 Cedex 5, France (e-mail: faybenb@hotmail.com).

J. F. Crouzet and B. Mohammadi are with Montpellier II University, Mathematics and Modeling Institute, Place Eugène Bataillon, Montpellier 34095 Cedex 5, France.

C. Comtat is with the Department of Medical Research, SHFJ, CEA, 91401 Orsay, France.

M. Fourcade and D. Mariano-Goulart are with Montpellier Medical University, Biophysics and Nuclear Medicine Department, Service de Médecine Nucléaire, CHU Lapeyronie, Montpellier 34295 Cedex 5, France.

Digital Object Identifier 10.1109/TMI.2007.897362

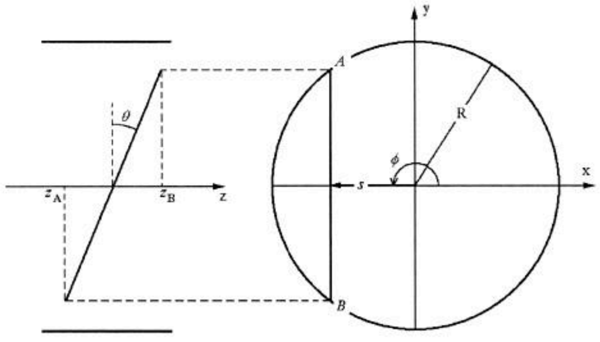

Fig. 1. Geometry of a PET scanner. Left: longitudinal section showing the axial variables z and θ. Right: transaxial view. The standard sinogram variables s and ϕ parameterize the straight line AB.

MRI [20]–[22] and the PET literature [23], [24], the results that have been published regarding gridding interpolation have renewed the interest of these DFM, thus increasing the need for fast and accurate methods providing complete 3-D projection data sets.

The aim of this paper was to start from the results of Defrise *et al.* [12], especially the analytical formula (FOREX), and to derive an extended relation in the 3-D Fourier space that would allow the estimation of any set of oblique projections from any other one. This led to a new reprojection method for estimating missing data that takes into account the whole set of projections measured by the scanner and thus allows a better handling of the data statistics. Furthermore, approximating the new 3-D analytical formula to the first order, we obtained an extended FORE equation that enabled us to derive an approximate reprojection algorithm as an alternative to the trivial "reverse" FORE method.

The validation study proposed in this paper was performed on simulated PET data. It aimed at testing whether these two new rebinning algorithms can be regarded as suitable alternatives to the "classical" rebinning methods used for the completion of 3-D PET data. These methods together with the new proposed rebinning algorithms were used as a preprocessing step before an exact 2-D rebinning using FOREX. Then, the 2-D rebinned sinograms were reconstructed and the resulting slices compared.

II. Extended Reprojection Formula

A. *Analytical Development*

Let us start (Fig. 1) with the expression of the weighted[1] line integral between two detectors of a distribution $f(x,y,z)$ of radioactive activity

$$p(s,\phi,z,\delta) = \int_{-\infty}^{+\infty} dt\, f(s\cos\phi - t\sin\phi, s\sin\phi + t\cos\phi, z + t\delta) \quad (1)$$

where δ represents the tangent of the angle θ. A set of projections with constant δ is called a segment. We only consider positive values of δ as

$$p(s,\phi,z,-\delta) = p(-s,\phi+\pi,z,\delta). \quad (2)$$

[1]The LOR data are assumed to be weighted by a factor $\sqrt{1+\tan^2\theta}$.

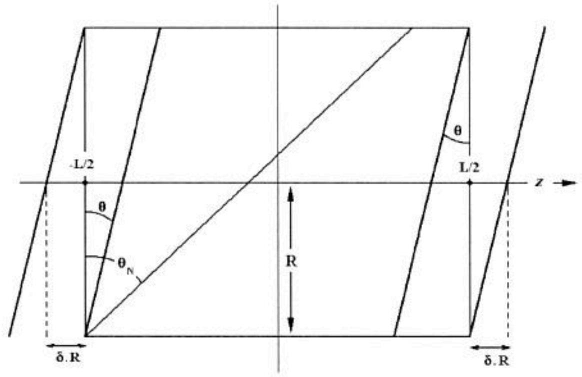

Fig. 2. The problem of the missing projections in the set of measured data: only segment $0(\delta = \tan\theta = 0)$ is axially invariant. Here, $\theta_N = \operatorname{atan}(\delta_N)$ is the aperture of the scanner, with δ_N the maximum ring difference.

The 2-D data corresponding to a couple (z,δ) is called a sinogram. The variable δ, which increases proportionally with the axial distance $|z_{\mathrm{A}} - z_{\mathrm{B}}|$ between the two detector rings in coincidence, is called the ring difference and is sampled from δ_0 to δ_{N}, the maximum ring difference. The sinograms gathered in the segment corresponding to $\delta_0 = 0$ are called transverse sinograms; the others are called oblique.

In order to be complete (axially invariant), a segment must gather all the projections in the range[2] (see Fig. 2)

$$|z| \leq \frac{L}{2} + \delta.R. \quad (3)$$

Due to the acquisition geometry (the finite length of the scanner), the projections are effectively recorded in the range:[3]

$$|z| \leq \frac{L}{2} - \delta.R. \quad (4)$$

When a set of projections $p(s,\phi,z,\delta)$ is axially invariant, its 3-D Fourier transform with respect to its first three variables writes

$$\wp(\omega,k,\zeta,\delta) = \int_{-\mathrm{R}}^{\mathrm{R}} ds \int_{0}^{2\pi} d\varphi \int_{-L/2}^{L/2} dz \times \exp(-ik\varphi - i\omega s - i\zeta z).p(s,\phi,z,\delta). \quad (5)$$

The FOREPROJ formula [12], [14], which can be derived from (5), gives us a means to express a set of oblique projections in terms of the transverse ones in the 3-D Fourier space

$$\wp(\omega,k,\zeta,\delta) = \exp\left(-ik\operatorname{atan}\left(\frac{\delta\zeta}{\omega}\right)\right)\wp(\omega^*,k,\zeta,0)$$
$$\text{with} \quad \omega^{*2} = \omega^2 + \delta^2\zeta^2. \quad (6)$$

[2]Actually, the range should be $|z| \leq L/2 + \delta\sqrt{R^2 - s^2}$, but for simplicity we consider the maximum range that is independent of s.

[3]The range should be $|z| \leq L/2 + \delta\sqrt{R^2 - s^2}$, but we consider the minimum range that is independent of s.

Let us rewrite (6) for two values of the ring difference, δ_1 and δ_2. One has

$$\begin{aligned}\wp(\omega^*, k, \zeta, 0) &= \exp\left(ik \text{ atan}\left(\frac{\delta_1\zeta}{\omega_1}\right)\right).\wp(\omega_1, k, \zeta, \delta_1)\\ &= \exp\left(ik \text{ atan}\left(\frac{\delta_2\zeta}{\omega_2}\right)\right).\wp(\omega_2, k, \zeta, \delta_2)\\ \text{with}\quad \omega^{*2} &= \omega_1^2 + \delta_1^2\zeta^2 = \omega_2^2 + \delta_2^2\zeta^2. \end{aligned} \tag{7}$$

Assuming that $\delta_1 > \delta_2$, we can then state that

$$\wp(\omega_1, k, \zeta, \delta_1) = \exp(-i\Delta\Phi).\wp(\omega_2, k, \zeta, \delta_2) \tag{8}$$

where

$$\omega_2 = \omega_1.\chi, \quad \chi = \sqrt{1 + \frac{\zeta^2}{\omega_1^2}(\delta_1^2 - \delta_2^2)} \tag{9}$$

and

$$\begin{aligned}\Delta\Phi &= k.\left(\text{atan}\left(\frac{\zeta\delta_1}{\omega_1}\right) - \text{atan}\left(\frac{\zeta\delta_2}{\omega_2}\right)\right)\\ &= k.\text{atan}\left(\zeta\frac{\delta_1^2 - \delta_2^2}{\delta_1\omega_1 + \delta_2\omega_2}\right).\end{aligned} \tag{10}$$

B. Zero-Order and First-Order Approximation

Since the ring difference δ is generally rather low for the usual clinical PET scanners, let us consider the "high-frequency" case and make the assumption that $\zeta\delta_1$ and $\zeta\delta_2$ are negligible, comparatively with ω_1 and ω_2. If we denote $\alpha = \zeta\delta/\omega$, where δ can be either δ_1 or δ_2, and ω stands for either ω_1 or ω_2, we can rewrite the frequency scaling χ and the phase shift $\Delta\Phi$ in terms of their Taylor expansion.

A zeroth order approximation gives us

$$\chi = 1 + O(\alpha^2) \approx 1, \quad \Delta\Phi = k.O(\alpha) = 0. \tag{11}$$

And after the inverse 3-D Fourier transform, one finds

$$p(s, \phi, z, \delta_1) = p(s, \phi, z, \delta_2) \tag{12}$$

which can be seen as an SSRB approximation that establishes an equivalence between the sinograms (z, δ), $\forall\delta \in [0, \delta_N]$.

The first-order approximation leads to

$$\chi = 1 + O(\alpha^2) \approx 1 \text{ so that } \omega_1 = \omega_2 = \omega \tag{13}$$

$$\Delta\Phi = k\zeta\left(\frac{\delta_1}{\omega_1} - \frac{\delta_2}{\omega_2}\right) + O(\alpha^3) \approx \frac{k\zeta}{\omega}(\delta_1 - \delta_2) \tag{14}$$

and (8) becomes

$$\wp(\omega, k, \zeta, \delta_1) \approx \exp\left(-ik\frac{(\delta_1 - \delta_2)\zeta}{\omega}\right)\wp(\omega, k, \zeta, \delta_2). \tag{15}$$

Noting P the 2-D Fourier transform of p with respect to its first two variables, we can simplify (15) by taking its 1-D inverse Fourier transform with respect to z. One obtains

$$P(\omega, k, z, \delta_1) \approx P\left(\omega, k, z - \frac{k(\delta_1 - \delta_2)}{\omega}, \delta_2\right). \tag{16}$$

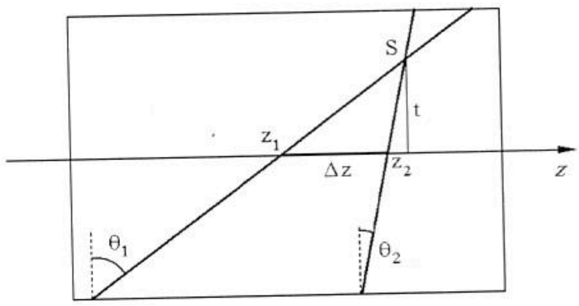

Fig. 3. Geometrical interpretation with the frequency-distance principle. S is a virtual source that contributes to the couple (ω, k) in both sinograms (z_1, δ_1) and (z_2, δ_2).

This formulation can be seen as an extension of the FORE approximation that relates the 2-D Fourier transforms of two sets of oblique projections. Setting $\delta_2 = 0$, we find the classical FORE formulation [11] that links the 2-D Fourier transform of an oblique set of projections with the 2-D transform of the transverse ones

$$P(\omega, k, z, \delta) \approx P\left(\omega, k, z - \frac{k\delta}{\omega}, 0\right) \tag{17}.$$

It should be noted that (16) can be regarded as a consequence of the *frequency-distance principle*, which is a property of the 2-D Radon transform first deduced by Edholm *et al.* [25]. This principle states that the value of the 2-D Fourier transform $P(\omega, k, z, \delta)$ of a sinogram at the pair of frequencies (ω, k) receives a main contribution from sources S located at a fixed distance $t = -k/\omega$ from the axis, along the lines of integration (see Fig. 3).

From this point of view, we can consider that a source S contributing to the pair (ω, k) in a certain sinogram (z_1, δ_1) provides the same contribution, for the same couple of frequencies, to the sinogram (z_2, δ_2) where $z_2 = z_1 + \Delta z$.

The axial shift Δz follows easily from Fig. 3

$$\begin{aligned}\Delta z &= \text{t}(\tan\theta_1 - \tan\theta_2)\\ &= \text{t}(\delta_1 - \delta_2)\\ &= -k\frac{\delta_1 - \delta_2}{\omega}.\end{aligned} \tag{18}$$

III. Derived Algorithms for the Estimation of Oblique Data

A. Exact Algorithm

Let us consider a set of 3-D data $p(s, \phi, z, \delta)$ measured by a PET scanner. These data are recorded as a set of 2-D sinograms ($s \in [-\text{R}, \text{R}]$, $\phi \in [0, 2\pi[$), where each sinogram is indexed by two parameters

$$\delta \in [\delta_0 = 0, \delta_1, \ldots, \delta_\text{N}], \quad z \in \left[-\frac{L}{2} + \delta R, \frac{L}{2} - \delta R\right] \tag{19}$$

where R is the radius and L the length of the scanner. As stated in Section II, only the transverse projections are complete (axially invariant). For $\delta > 0$, a part of the data is missing, which corresponds to

$$\frac{L}{2} - \delta R < |z| \leq \frac{L}{2} + \delta R. \tag{20}$$

In the implementation of certain algorithms (FOREX, 3DRP), it is essential to first estimate these missing projections in order to merge them with the original and reconstruct segments that are axially invariant.

In [12] and [14], the use of FOREPROJ (6) was proposed to estimate the oblique data on the basis of the set of transverse projections $p(s, \phi, z, 0)$.

From (8), we can derive another method that will be called in what follows "iterative FOREPROJ"

- The projections $p(s, \phi, z, 0)$ being complete, (8) enables us to compute (as with FOREPROJ) the projections with $\delta = \delta_1$.
- This estimation of $p(s, \phi, z, \delta_1)$ is merged on the range $|z| > L/2 - \delta_1.R$ with the data acquired by the scanner (the data actually acquired by the scanner remain unchanged). This provides us with a complete set of projections $p(s, \phi, z, \delta_1)$.
- Equation (8) gives us two different estimations of $p(s, \phi, z, \delta_2)$, based on our two axially invariant segments (0 and 1), which are averaged.
- The estimation of $p(s, \phi, z, \delta_2)$ is merged on the range $|z| > L/2 - \delta_2.R$ with the acquired data and the process goes on iteratively until the missing data in the segment corresponding to $\delta = \delta_N$ are estimated from segments $[0 \ldots \delta_{N-1}]$.

These two exact methods imply 1-D linear interpolation while performing the frequency scaling from ω_1 to ω_2. Radial zero-padding can be achieved in order to minimize the effect of the interpolations [14]; however, since our goal is to compare these two FOREPROJ algorithms, we did not use zero-padding.

B. Approximate Algorithm

As the implementation of the first-order approximation (16), (17) no longer requires the axial invariance of the data (no Fourier transform in the axial direction), there are roughly two ways of exploiting this approximation for the estimation of missing oblique projections.

- A straightforward implementation of (17) yields a method that computes the oblique data $p(s, \phi, z, \delta)$, $\delta \in [\delta_1 \delta_N]$ from the transverse ones. Let us name this method "reverse FORE."
- Equation (16) provides an alternative that we will call in what follows "extended FORE:" for each missing oblique sinogram (z, δ), such that $|z| > \mathrm{L}/2 - \delta.R$, $P(\omega, k, z, \delta)$ can be approximated by $P(\omega, k, z + \Delta z, \delta')$, with $\Delta z = k(\delta' - \delta)/\omega$, for $\delta' \in [\delta_0\ \delta_N]$. Provided that every $(z + \Delta z, \delta')$ sinogram has been recorded, this yields up to $N + 1$ different estimations that can be averaged to compute $p(s, \phi, z, \delta)$.

As (16) and (17) are both "high-frequency" approximations, their validity vanishes when the first-order approximation is no longer acceptable [12]. In this case, the first-order approximation is replaced with the zeroth-order approximation SSRB (12) for which the axial shift Δz vanishes.

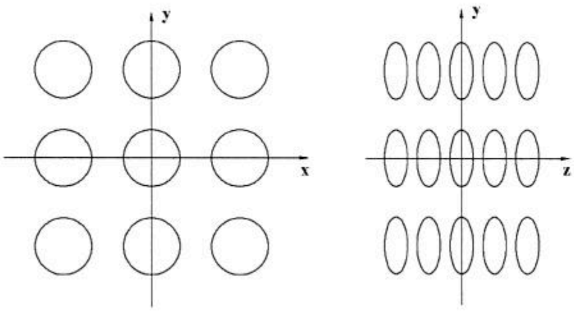

Fig. 4. The chosen phantom is constituted of 45 ellipsoids of half-axes (50 mm, 50 mm, 12 mm). Here are displayed the (x, y) and the (y, z) views.

IV. Materials and Methods

We tested the above algorithms on simulated data. The chosen phantom (Fig. 4) is constituted of 45 ellipsoids situated by groups of nine in the transaxial planes corresponding to $z = -61.6, -30.8$, 0, 30.8, and 61.6 (mm). Their axial half-axis is 12 mm. In each transaxial plane, their centers are located at $(x, y) = (-150, 0, 150) \times (-150, 0, 150)$. Their transaxial half-axes are 50 mm. Their activity is fixed to 1 over a 0 background activity.

The projections were analytically simulated [26], assuming no attenuation and equidistant parallel projections, for the HIREZ scanner, which is approximated as a 39-ring scan with an aperture of 8.6°. The maximum index difference between two detectors in coincidence for a recorded LOR is 31, and the span (axial compression) is 3, which leads to a δ-sampling of $\delta_n = 0.0151\, n, n = 0 \ldots N\ (N = 10)$. The axial field-of-view (FOV) is 161.8 mm and the transaxial FOV radius is 321.6 mm.

Besides the noiseless simulation, Poisson noise was introduced into the data [26] in order to study the behavior of the algorithms under conditions of noisy acquisition. The total of the simulated net trues was 25 Mcounts. The noisy data were normalized so that the total recorded activity was the same as for the noiseless projections. In these two sets of projections, there are missing oblique data, as the software only simulates the data really acquired by the scanner. In order to judge the quality of the four methods in estimating these missing oblique data, we analytically computed the whole set of complete oblique projections that we call in what follows "exact data."

The initial sampling of the 2-D sinograms for the HIREZ scan is 312×312. These sinograms were re-sampled to 128×128, in order to carry out the FFTs, which leads to a pixel size of 5 mm $\times$ 5 mm. The axial (z) sampling was conserved: the transverse projections are constituted of 77 slices, which corresponds to a slice thickness of 2.075 mm. Zero-padding was achieved in the axial direction in order to bring the number of samples to 128.

V. Results

The oblique projections corresponding to $\delta = \delta_1, \delta_2, \ldots, \delta_N$ were estimated for both the noiseless and noisy data, using the four methods described in Section III. These estimated oblique

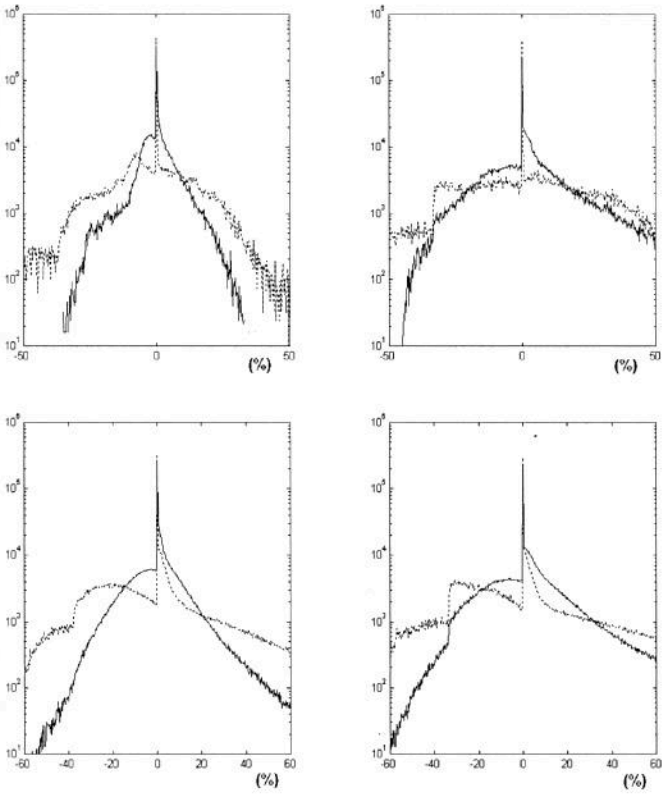

Fig. 5. Histogram of the difference (normalized to the data maximum) between the exact sinograms and the sinograms estimated from (top) noiseless and (bottom) noisy data. Comparison between reverse FORE (dashed) and extended FORE (solid). Left: ring difference: δ_3. Right: ring difference: δ_{10}.

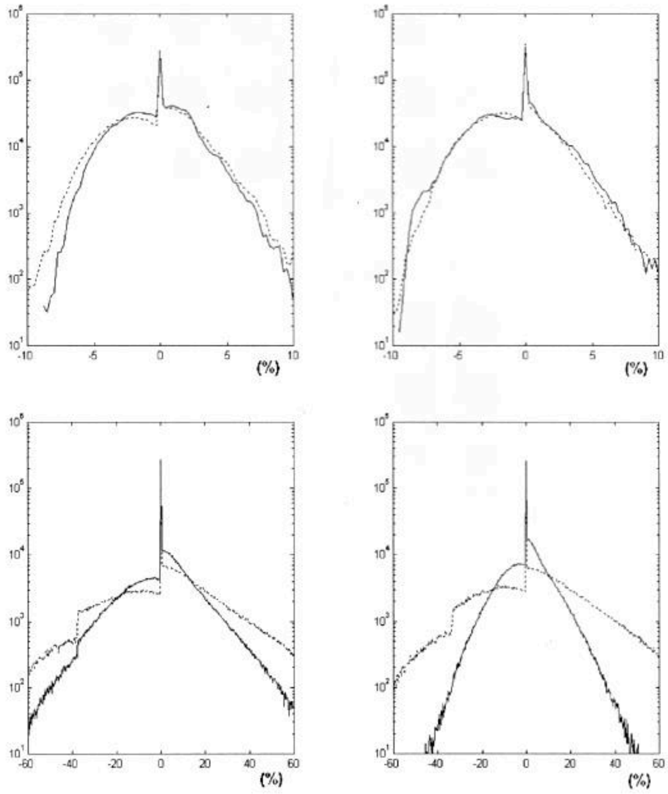

Fig. 6. Histogram of the difference (normalized to the data maximum) between the exact sinograms and the sinograms estimated from (top) noiseless and (bottom) noisy data. Comparison between FOREPROJ (dashed) and iterative FOREPROJ (solid). Left: ring difference: δ_3. Right: ring difference: δ_{10}.

projections were compared with exact oblique projections for two values of the ring difference (δ_3 and δ_{10}). Figs. 5 and 6 show, in logarithmic scale, the histograms of the pixel difference between the exact sinograms and the sinograms estimated (before merging) from both noiseless (top) and noisy (bottom) projection data, using the four rebinning methods tested.

After the estimation stage, the calculated projections were merged on the range $|z| > L/2 - \delta R$ with the simulated ones, the latter being unchanged. The completed data were then used to run the FOREX algorithm, which rebins the oblique data into transverse sinograms. The rebinned 2-D transverse sinograms were processed using a 2-D-FBP algorithm to reconstruct the 2-D images. When processing the noisy data, the frequency cutoff of the ramp filter was fixed to 60% of the Nyquist frequency.

The next two figures intend to exhibit the intrinsic influence of each method on the spatial resolution: Figs. 7 and 8 show radial and axial line profiles through the object reconstructed from noiseless data.

Figs. 9 and 10 illustrate the noise performance of the four methods by comparing the relative standard deviation in the reconstructed ellipsoids (normalized to the mean pixel value in the ellipsoid). Fig. 9 corresponds to the two approximate methods and Fig. 10 to the two exact ones.

Figs. 11–14 are proposed to give an insight into the reconstructed images when working with noiseless data (Figs. 11 and 12) and noisy projection data (25 million total trues simulated, Figs. 13 and 14). Figs. 11 and 13 show the reconstruction of an "external" slice ($z = -61.6$ mm), these slices being the more affected by the errors committed during the missing data estimation. As for Figs. 12 and 14, they allow an axial appreciation of the reconstructed object by showing the (y, z) views corresponding to $x = 0$ mm. These (y, z) views are not isotropic as they are simply extracted from the stack of 2-D (x, y) views (with a voxel size of 5 mm$\times$5 mm$\times$2.075 mm). On Figs. 13 and 14, the contour lines at 20% of the slice maximum superimposed on the grey scale images give an idea of the contrast in the reconstructed object. On each figure, from top left to bottom right, the four images refer to the object reconstructed with missing projections estimated using, respectively, reverse FORE, extended FORE, FOREPROJ, and iterative FOREPROJ.

Finally, Table I illustrates the computational cost of each method for the considered case: HIREZ scanner with 11 values of δ, and a (s, ϕ, z) sampling of $128 \times 128 \times 128$ (after resampling in the s and ϕ variables, and zero-padding in the z direction). These times do not include the FOREX rebinning nor the 2-D reconstruction.

VI. Discussion

It appears clearly from Fig. 5 that, from both noiseless and noisy projection data, extended FORE allows a better estimation of the oblique sinograms than reverse FORE. The difference between the two methods does not depend on the ring difference, which is understandable since the statistics that are exploited to estimate a segment is always the same (the nonoblique data

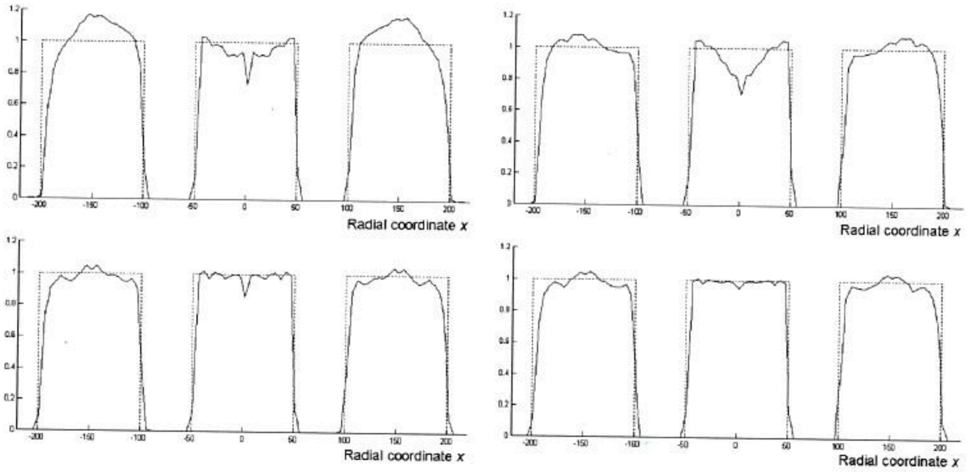

Fig. 7. Radial line profiles ($y = 0$ mm, $z = 61.6$ mm) through the object reconstructed from noiseless data. The dashed curves correspond to the exact line profile through the object. The completion was achieved using: top left: reverse FORE. Top right: extended FORE. Bottom left: FOREPROJ. Bottom right: iterative FOREPROJ.

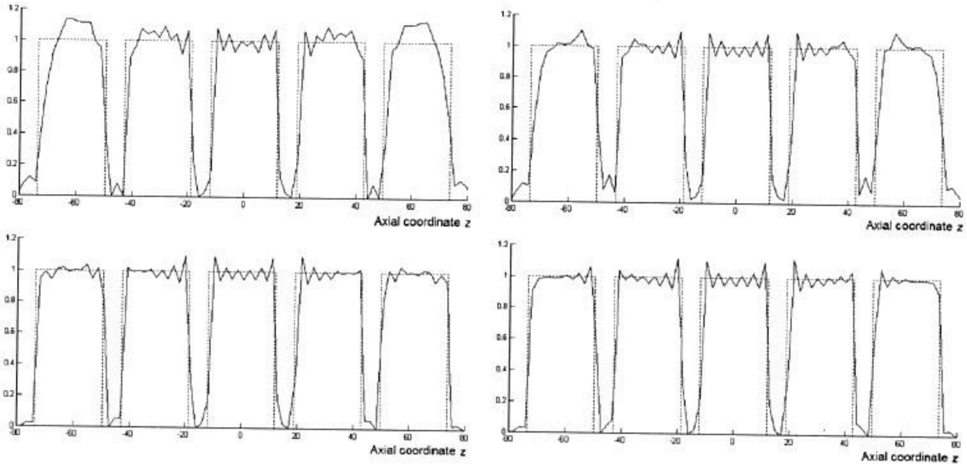

Fig. 8. Axial line profiles ($x = 0$ mm, $y = 150$ mm) through the object reconstructed from noiseless data. The dashed curves correspond to the exact line profile through the object. The completion was achieved using: top left: reverse FORE. Top right: extended FORE. Bottom left: FOREPROJ. Bottom right: iterative FOREPROJ.

when using reverse FORE, and the whole 3-D data when using extended FORE).

For what concerns the two exact methods, Fig. 6 shows that, when working with noiseless data and compared with FOREPROJ, iterative FOREPROJ does not substantially damage the quality of the estimated projections when δ increases. When working with noisy data, it appears that the exploitation of an increasing amount of data statistics enables an improvement in the quality of the estimations. This improvement becomes clearer when the ring difference increases.

It has to be noted that, after processing the sinograms, the pixels with a negative value are set to zero. This explains in part that the pixels initially having a 0 value are generally well estimated, leading to a pike in the histograms for the 0% difference.

Figs. 7 and 8 give an idea of the accuracy of the different methods while working with noiseless data. The radial line profiles show that the exploitation of the approximate methods leads to large radial artifacts in the external slices, i.e., an underestimation of the activity near the axis and an overestimation at the radial FOV border. The axial profiles exhibit axial smoothing due to the interpolations, as well as a loss of axial resolution for the ellipsoids situated in the planes $z = +/-61.6$ mm. The use of extended FORE, although it seems to reinforce the radial artifact on the axis, allows better radial and axial accuracy in the external slices

Concerning the two exact algorithms, the iterative implementation of FOREPROJ clearly preserves the quality of the radial profile through the reconstructed slice, as well as the spatial resolution along the axial direction z that was achieved using classical FOREPROJ.

As expectable, the main advantage of the two proposed algorithms (i.e., a better handling of the data statistics) should lead to an improvement in the SNR in the reconstructed object when working with noisy low-statistics data. This is reflected in Figs. 9 and 10, which show the relative standard deviation in the reconstructed ellipsoids (in percent of the mean pixel value in the ellipsoid). Fig. 9 shows that the use of the extended FORE algorithm allows SNR improvement near the scanner axis. This improvement gradually increases when approaching the axial FOV border (60%–65% standard deviation with reverse FORE versus 45%–50% with extended FORE).

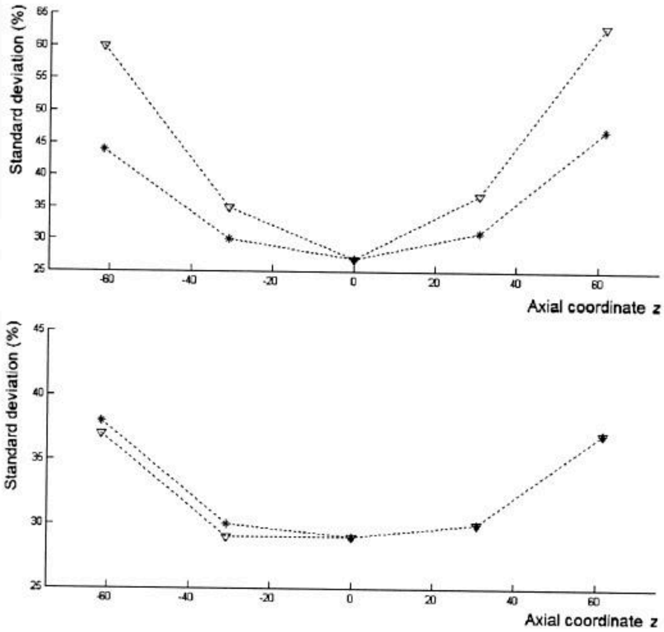

Fig. 9. Standard deviation calculated in the reconstructed ellipsoids (normalized to the mean pixel value in the ellipsoid) after completion using (triangles) reverse FORE and (stars) extended FORE. Top: ellipsoids situated on the scanner axis ($x = 0$ mm, $y = 0$ mm). Bottom: ellipsoids situated off-axis ($x = 150$ mm, $y = 150$ mm).

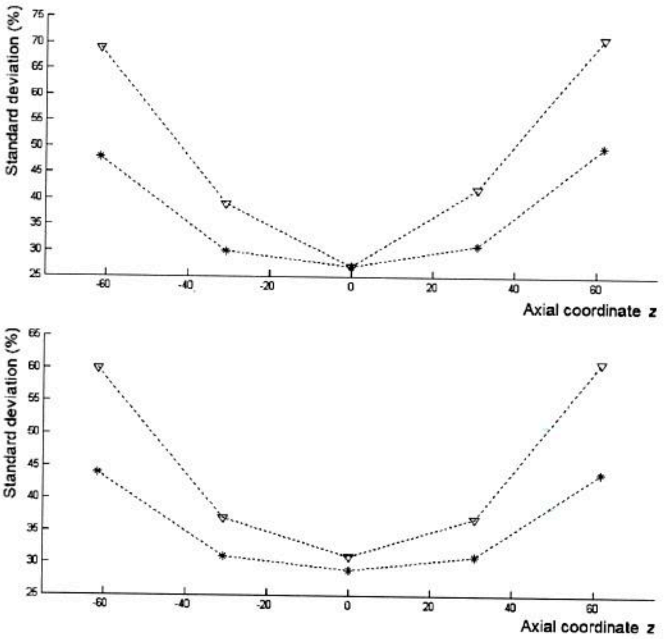

Fig. 10. Standard deviation calculated in the reconstructed ellipsoids (normalized to the mean pixel value in the ellipsoid) after completion using (triangles) FOREPROJ and (stars) iterative FOREPROJ. Top: ellipsoids situated on the scanner axis ($x = 0$ mm, $y = 0$ mm). Bottom: ellipsoids situated off-axis ($x = 150$ mm, $y = 150$ mm).

Fig. 10 shows that the iterative implementation of FOREPROJ allows significant SNR improvement over the whole radial FOV. This improvement gradually increases when reaching the scanner edge, where the quality of the estimated oblique data becomes determinant.

The four figures presenting reconstructed slices allow a more qualitative assessment of the tested methods. The noiseless

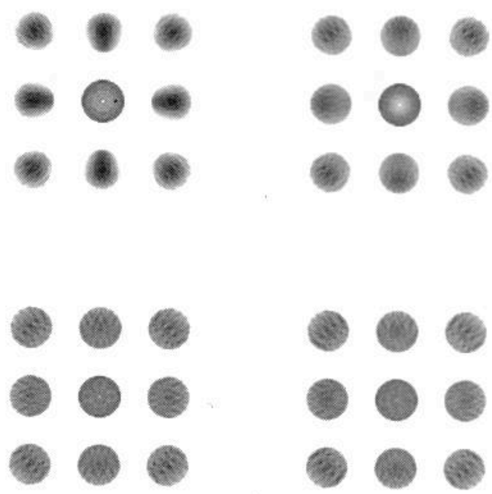

Fig. 11. (x, y) views of the object reconstructed with noiseless data. The slice corresponds to $z = -61.6$ mm. The missing data are estimated using: top left: reverse FORE. Top right: extended FORE. Bottom left: FOREPROJ. Bottom right: iterative FOREPROJ.

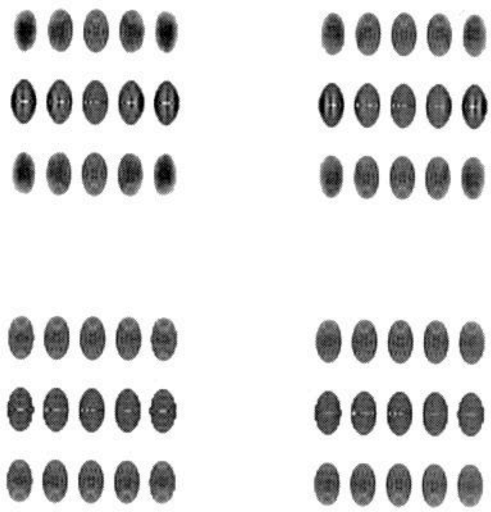

Fig. 12. (y, z) views of the object reconstructed with noiseless data. The slice corresponds to $x = 0$ mm. The missing data are estimated using: top left: reverse FORE. Top right: extended FORE. Bottom left: FOREPROJ. Bottom right: iterative FOREPROJ.

TABLE I
REPRESENTATIVE COMPUTATIONAL COSTS

Method	Computation time
Reverse FORE	0' 53''
Extended FORE	1' 50''
FOREPROJ	3' 18''
Iterative FOREPROJ	13' 27''

slices confirm the presence of large radial and angular artifacts in the external slices of the object preprocessed with the approximate rebinning algorithms. It appears, however, that extended FORE enables a better recovery of the object contours, except along the scanner axis. Concerning the two FOREPROJ methods, they do not cause evident artifacts and lead to similar reconstructions with noiseless data. As for Figs. 13 and 14, they clearly illustrate the results previously deduced from Figs. 9, 10 concerning the enhanced SNR on the axial FOV border.

Finally, Table I shows the gain in computation time that can be achieved when using approximate algorithms: there is about

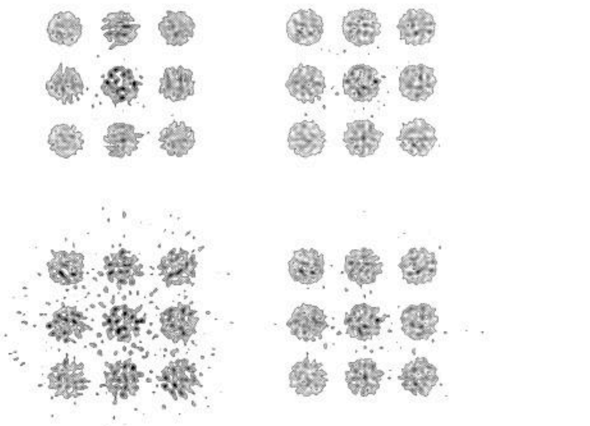

Fig. 13. The (x, y) views of the object reconstructed with noisy data (25 Mkps). The slice corresponds to $z = -61.6$ mm. The missing data are estimated using: top left: reverse FORE. Top right: extended FORE. Bottom left: FOREPROJ. Bottom right: iterative FOREPROJ. The contour at 20% of the slice maximum is superimposed.

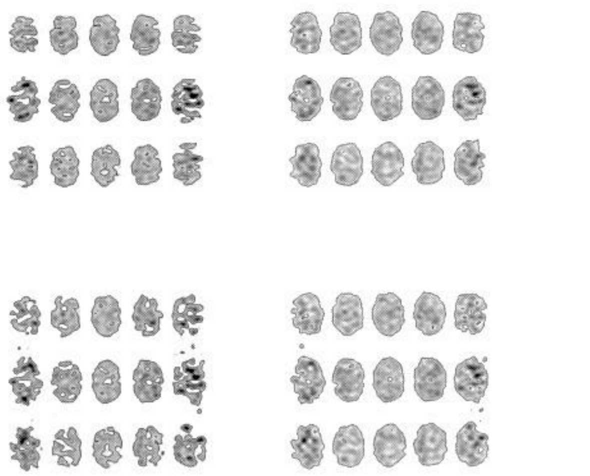

Fig. 14. The (y, z) views of the object reconstructed with noisy data (25 Mkps). The slice corresponds to $x = 0$ mm. The missing data are estimated using: top left: reverse FORE. Top right: extended FORE. Bottom left: FOREPROJ. Bottom right: iterative FOREPROJ. The contour at 20% of the slice maximum is superimposed.

a factor of 4–7 when passing from FORPROJ to reverse FORE or from iterative FOREPROJ to extended FORE.

VII. Conclusion

From the analytical FOREX formula of Defrise *et al.*, we derived an iterative reprojection algorithm (iterative FOREPROJ) whose main advantage is better handling of the data statistics, compared with the classical FOREPROJ method. In first approximation, this leads to an approximate method that can be seen as an extended FORE reprojection technique.

After numerical simulation on the HIREZ scanner, the iterative FOREPROJ scheme provided a clear improvement in the quality of the estimated oblique data, compared with classical FOREPROJ. Iterative FOREPROJ allowed better recovery and an SNR rise in the external slices of the reconstructed object. The propagation of the systematic interpolation errors along with the iterations does not seem to have a harmful influence on the spatial resolution of the reconstructed images.

Concerning the extended FORE approximation, although it provides progressive SNR enhancement along the scanner axis compared with the reverse FORE implementation, the artifacts implied by the axial interpolation had a noticeable impact on the quality of the estimated data, probably due to the geometry of the phantom studied. However, this approximate method should prove its efficiency with axially smoother projection data and needs to undergo clinical studies with more realistic measured data in order to determine its pertinence.

Last, further theoretical and clinical studies are now necessary to test the iterative FOREPROJ and the extended FORE algorithms as preprocessing tools to complete the 3-D sinograms that are to be processed by fully 3-D algorithms (3DRP or DFMs).

Acknowledgment

The authors would like to thank the anonymous reviewers for their valuable comments and suggestions.

References

[1] J. G. Colsher, "Fully three-dimensional positron emission tomography," *Phys. Med. Biol.*, vol. 25, pp. 103–105, 1980.

[2] J. G. Rogers, R. Harrop, and P. E. Kinahan, "The theory of three-dimensional image reconstruction for PET," *IEEE Trans. Med. Imag.*, vol. 6, pp. 239–243, 1987.

[3] D. W. Townsend, T. Spinks, T. Jones, A. Geissbuhler, M. Defrise, M. C. Gilardi, and J. Heather, "Three-dimensional reconstruction of PET data from a multi-ring camera," *IEEE Trans. Nucl. Sci.*, vol. 36, no. 1, pp. 1056–1066, Feb. 1989.

[4] P. E. Kinahan and J. G. Rogers, "Analytic three-dimensional image reconstruction using all detected events," *IEEE Trans. Nucl. Sci.*, vol. 36, pp. 964–968, 1990.

[5] M. W. Stazyk, J. G. Rogers, and R. Harrop, "Full data utilization in PVI using the 3-D Radon transform," *Phys. Med. Biol.*, vol. 37, pp. 689–704, 1992.

[6] P. E. Kinahan and J. S. Karp, "Figures of merit for comparing reconstruction algorithms with a volume-imaging PET scanner," *Phys. Med. Biol.*, vol. 39, pp. 631–642, 1994.

[7] S. Matej and R. M. Lewitt, "3-D-FRP: Direct Fourier reconstruction with Fourier reprojection for fully 3-D PET," *IEEE Trans. Nucl. Sci.*, vol. 48, no. 4, pp. 1378–1385, Aug. 2001.

[8] M. E. Daube-Witherspoon and G. Muehllehner, "Treatment of axial data in three-dimensional PET," *J. Nucl. Med.*, vol. 28, pp. 1717–1724, 1987.

[9] R. M. Lewitt, G. Muehllehner, and J. S. Karp, "Three-dimensional reconstruction for PET by multi-slice rebinning and axial image filtering," *Phys. Med. Biol.*, vol. 39, pp. 321–340, 1994.

[10] K. Erlandsson, P. D. Esser, S.-E. Strand, and R. L. Van Heertum, "3-D reconstruction for a multi-ring PET scanner by single-slice rebinning and axial deconvolution," *Phys. Med. Biol.*, vol. 39, pp. 619–629, 1994.

[11] M. Defrise, "A factorization method for the 3-D X-ray transform," *Inverse Problems*, vol. 11, pp. 983–994, 1995.

[12] M. Defrise, P. E. Kinahan, D. W. Townsend, C. Michel, M. Sibomana, and D. F. Newport, "Exact and approximate rebinning algorithms for 3-D PET data," *IEEE Trans. Med. Imag.*, vol. 16, no. 2, pp. 145–158, Apr. 1997.

[13] E. Tanaka and Y. Amo, "A Fourier rebinning algorithm incorporating spectral transfer efficiency for 3-D PET," *Phys. Med. Biol.*, vol. 43, pp. 739–746, 1998.

[14] X. Liu, M. Defrise, C. Michel, M. Sibomana, C. Comtat, P. E. Kinahan, and D. W. Townsend, "Exact rebinning methods for three-dimensional positron tomography," *IEEE Trans. Med. Imag.*, vol. 18, no. 8, pp. 657–664, Aug. 1999.

[15] M. Defrise, X. , and Liu, "A fast rebinning algorithm for 3-D PET using John's equation," *Inverse Problems*, vol. 15, pp. 1047–1065, 1999.

[16] V. Sossi, M. W. Stazyk, P. E. Kinahan, and T. J. Ruth, "The performance of the single-slice rebinning for imaging the human striatum as evaluated by phantom studies," *Phys. Med. Biol.*, vol. 39, pp. 369–380, 1994.

[17] P. E. Kinahan, "Image reconstruction algorithms for volume imaging PET scanners," Ph.D. dissertation, Univ. Pennsylvania, Philadelphia, PA, 1994.

[18] M. Defrise, A. Geissbuhler, and D. W. Townsend, "A performance study of 3-D reconstruction algorithms for PET," *Phys. Med. Biol.*, vol. 39, pp. 321–340, 1994.

[19] S. Matej, J. S. Karp, R. M. Lewitt, and A. J. Becher, "Performance of the Fourier rebinning algorithm for the 3-D PET with large acceptance angles," *Phys. Med. Biol.*, vol. 43, pp. 787–797, 1998.

[20] C. H. Meyer, B. S. Hu, D. G. Nishimura, and A. Macovski, "Fast spiral coronary artery imaging," *Magn. Reson. Med.*, vol. 28, pp. 202–213, 1992.

[21] D. C. Noll, "Multishot rosette trajectories for spectrally selective MR imaging," *IEEE Trans. Med. Imag.*, vol. 16, no. 4, pp. 372–377, Aug. 1997.

[22] J. G. Pipe and P. Menon, "Sampling density compensation in MRI: Rationale and an iterative numerical solutions," *Magn. Reson. Med.*, vol. 41, no. 1, pp. 179–186, 1999.

[23] J. A. Fessler and B. P. Sutton, "Non uniform fast Fourier transforms using min-max interpolation," *IEEE Trans. Signal Process.*, vol. 51, no. 2, pp. 560–574, Feb. 2003.

[24] S. Matej and I. G. Kazantsev, "Fourier-based reconstruction for Fully 3-D PET: Optimization of interpolation parameters," *IEEE Trans. Med. Imag.*, vol. 25, no. 7, pp. 845–854, Jul. 2006.

[25] P. R. Edholm, R. M. Lewitt, and B. Lindholm, "Novel properties of the Fourier decomposition of the sinogram," *Proc. SPIE The Int. Soc. Opt. Eng*, vol. 671, pp. 8–18, 1986.

[26] C. Comtat, P. Kinahan, M. Defrise, C. Michel, C. Lartizien, and D. Townsend, "Simulating whole-body PET scanning with rapid analytical methods," in *Proc. IEEE Nucl. Sci. Symp. Med. Imag. Conf.*, Seattle, WA, Oct. 1999, vol. 3, pp. 1260–1264.